IEEE Photonics Journal
An IEEE Photonics Society Publication

A Short-Wave Infrared Nanoinjection Imager With 2500 A/W Responsivity and Low Excess Noise

Volume 2, Number 5, October 2010

O. G. Memis, Member, IEEE
John Kohoutek, Student Member, IEEE
Wei Wu, Student Member, IEEE
Ryan M. Gelfand, Student Member, IEEE
Hooman Mohseni, Senior Member, IEEE

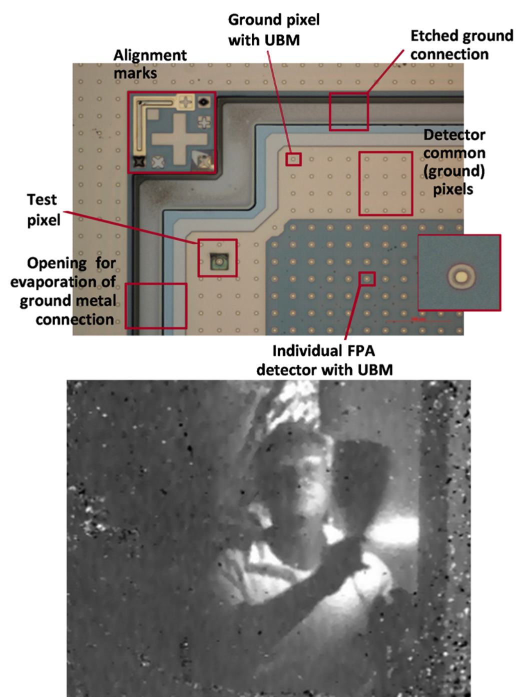

DOI: 10.1109/JPHOT.2010.2073695
1943-0655/$26.00 ©2010 IEEE

IEEE photonics SOCIETY

IEEE

A Short-Wave Infrared Nanoinjection Imager With 2500 A/W Responsivity and Low Excess Noise

Omer Gokalp Memis, *Member, IEEE*,
John Kohoutek, *Student Member, IEEE*,
Wei Wu, *Student Member, IEEE*,
Ryan M. Gelfand, *Student Member, IEEE*,
and Hooman Mohseni, *Senior Member, IEEE*

Department of Electrical Engineering and Computer Science,
Northwestern University, Evanston, IL 60202 USA

DOI: 10.1109/JPHOT.2010.2073695
1943-0655/$26.00 ©2010 IEEE

Manuscript received June 25, 2010; revised August 30, 2010; accepted August 30, 2010. Date of publication September 7, 2010; date of current version September 24, 2010. Corresponding author: O. G. Memis (e-mail: gokalp@northwestern.edu).

Abstract: We report on a novel nanoinjection-based short-wave infrared imager, which consists of InGaAs/GaAsSb/InAlAs/InP-based nanoinjection detectors with internal gain. The imager is 320×256 pixels with a 30-μm pixel pitch. The test pixels show responsivity values in excess of 2500 A/W, indicating generation of more than 2000 electrons/photon with high quantum efficiency. This amplification is achieved at complementary metal-oxide semiconductor (CMOS) compatible, subvolt bias. The measured excess noise factor F of the hybridized imager pixels is around 1.5 at the responsivity range 1500 to 2000 A/W. The temperature behavior of the internal dark current of the imager pixels is also studied from 300 to 77 K. The presented results show, for the first time, that the nanoinjection mechanism can be implemented in imagers to provide detector-level internal amplification, while maintaining low noise levels and CMOS compatibility.

Index Terms: Imaging, imaging system.

1. Introduction

Improving sensitivity in the infrared spectrum is a challenging task due to the minute energy of each photon at less than 1 aJ. An important part of the infrared spectrum is the short-wave infrared (SWIR), which is used in many applications including telecommunications, biophotonics [1], optical tomography [2], explosives detection [3], and nondestructive material evaluation [4]. It includes the fiber optic telecommunications wavelengths around 1.5 μm, and can advance rapidly emerging technologies like quantum key distribution [5] and quantum computing [6], [7]. Furthermore, many medical applications like optical tomography rely on SWIR since it has great penetration depth through the skin [8] and, therefore, enables deeper noninvasive screening. Additionally, night sky radiance [9] offers significant spectral power in SWIR due to the chemical reactions involving hydroxyl groups in the upper atmosphere [10]. This phenomenon makes SWIR uniquely attractive for military and homeland security applications.

In order to improve the detection sensitivity in SWIR applications, the *nanoinjection detector* was developed, which utilizes an avalanche-free detection and amplification mechanism [11]. The nanoinjection detector is based on a type-II material system, i.e., InP/GaAsSb/InAlAs/InGaAs. This structure presents a barrier in conduction band and a trap in the valance band. When the device is

biased, the electrons in the highly doped InP layer are attracted toward the InGaAs absorption region; however, their transport is limited by the conduction band barrier.

Upon photon absorption, an electron-hole pair is generated in the large InGaAs absorption region. Due to the internal electric field, holes are attracted to the nanoinjector that has a type-II band alignment with InP and InGaAs and presents a trap for holes. The small volume of the trap represents a low capacitance, and when one single hole is trapped in the sensitive nanovalve (nanoinjector), it will lower the barrier and release thousands of electrons, which is similar to a single electron transistor [12]. The large absorption region ensures that the incoming photons are captured with high efficiency, and we estimate the internal quantum efficiency of each detector to exceed 85% based on the absorption coefficient of InGaAs and thickness of the layers.

In addition to high quantum efficiency, the nanoinjection mechanism offers other advantages. Due to the internal amplification mechanism, the signals get boosted within the detector, making them more immune to the downstream noise sources such as amplifiers or analog-to-digital converters. Moreover, the nanoinjection amplification mechanism itself is also low noise, as it relies on a negative internal feedback to stabilize the injection/amplification. This negative feedback is created by the injected electrons counterbalancing the trapped holes in GaAsSb barrier/trap layer. In addition to the trapped holes lowering the barrier, the injected electrons also slightly influence the barrier in the opposite direction, thereby creating a dynamic equilibrium. The dynamic equilibrium prevents temporal bunching of carriers and, hence, lowers the noise levels. This results in the Fano effect [13], where a negative feedback stabilizes the current flow.

Here, we present our first imager results, showing the potential of nanoinjection technology, to provide high-fidelity internal amplification with small pixel sizes (30 μm pitch) and a large number of pixels (320 $\times$ 256 pixels). The only other solid-state photodetector platform that can provide linear-mode internal amplification is an avalanche photodetector (APD). However, APDs require a high electric field and guard rings to prevent breakdown, which increase the size of detectors [14] and imager pixels. Hence, it is difficult to achieve a high factor and small pitch that is less than 50 μm. Furthermore, the large bias voltage requirements of APD make them incompatible with CMOS devices such as read-out integrated circuits. For these reasons, realization of high-resolution imagers with high internal gain and low noise has remained a challenging task.

2. Nanoinjection Imager Fabrication

The hybridization presented a major challenge, as the read-out integrated circuitry (ROIC) was optimized for unity-gain PIN-based photodetectors. A compatible device structure was designed for maximum ROIC compatibility, together with a new process flow.

The nanoinjection imager chips were processed on epitaxial layers which were grown on 2-in InP substrates using metal organic chemical vapor deposition (MOCVD). From top to bottom, the epitaxial layers consist of 50-nm InGaAs $(10^{19}\ \text{cm}^{-3})$, 500-nm InP $(10^{17}\ \text{cm}^{-3})$, 50-nm InAlAs (undoped), 50-nm GaAsSb $(5 \times 10^{18}\ \text{cm}^{-3})$, 1000-nm InGaAs (undoped), and 50-nm InGaAs (graded doping). Wafers were patterned with photolithography to form the devices with 10-μm injectors, followed by a metal lift-off. With the metal as hard mask, a CH_4/H_2 reactive dry etching (RIE) process formed the injection detectors. Samples were passivated with SiO_2 using plasma-enhanced chemical vapor deposition. An under bump metallurgy (UBM) of Cr/Au/Ni was evaporated on each pixel. The indium bumps were electroplated using an Au seed layer, after which, the backside was polished. To remove the effects of the passivation layer, and to re-activate the device, a special RIE process was used, during which the passivation layer was etched using CF_4/O_2 plasma, and the surface quality was restored using $CH_4/H_2/Ar$ plasma.

Fig. 1 illustrates various sections of the imager chip, with areas for imager pixels, test pixels, ground pixels (connections), and alignment marks. In this design, the imager pixels form the infrared image, and the ground pixels connect the backside of the imager (detector common) to the read-out integrated circuit. The test pixels are connected to a fan-out, through which they can be individually tested. A scanning electron microscope (SEM) of the final imager pixels is shown in Fig. 2.

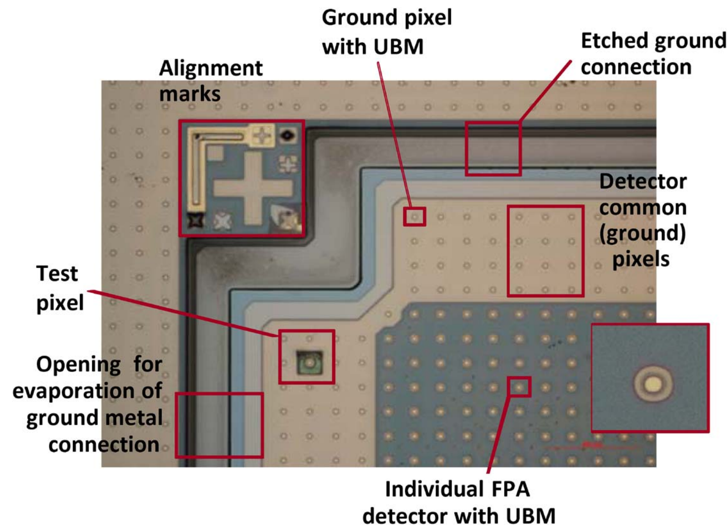

Fig. 1. Optical microscope image of the imager, showing different parts of the imager, including individual pixels with under bump metallurgy (UBM), test pixels with UBM, the detector common (ground) ridge, and alignment marks.

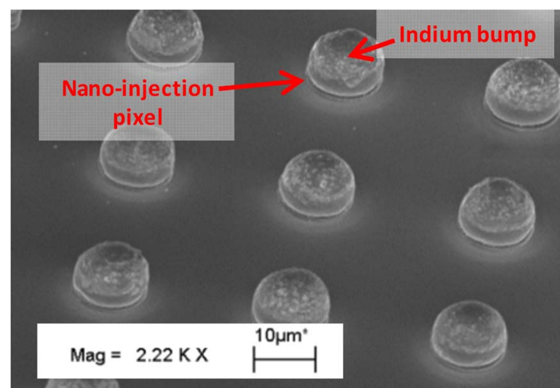

Fig. 2. SEM image of the processed nano-injection imagers with indium bumps on each pixel. Each pixel is 10 μm in diameter and has a UBM of Cr/Au/Ni. On top of the UBM, an indium bump of similar radius resides.

To realize the nanoinjection imager, we had to hybridize the 2-D 320$\times$256 pixel array of our nanoinjection detectors with an off-the-shelf silicon CMOS ROIC (ISC9705 from Indigo). The FPA and ROIC both have the same pixel pitch of 30 μm. Indium bumps were formed on the ROIC using a similar process of Indium electroplating on Au seed layer. The unpassivated focal plane array and ROIC were placed in a flip chip bonder (SET FC150). The hybridization was done with temperature ramped to 170 $^\circ$C for 60 s. The imager was wirebonded on a leadless chip carrier (LCC).

3. Measurements and Imaging

For current-voltage and noise measurements, the hybridized sample was placed in a custom-built visible/infrared microscope setup, which doubled as a beam collimator for the laser beam. A tunable laser source at $\lambda = 1.55$ μm was used as an optical source. The actual power reaching the sample was measured with a National Institute of Standards and Technology-calibrated PIN detector. In

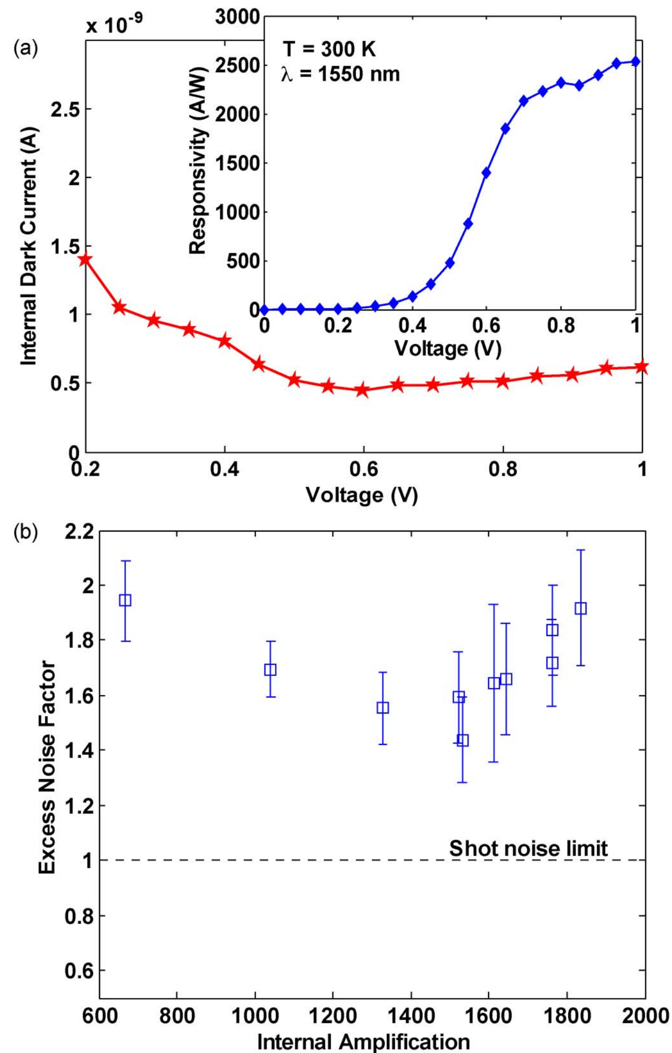

Fig. 3. (a) Internal dark current (before amplification) and responsivity versus voltage of a test pixel plotted at room temperature and $\lambda = 1550$ nm. (b) The excess noise factor F of the test pixel is around 1.5 at internal amplification values between 1200 and 1600.

each hybridized imager chip, four extra nanoinjection detectors with direct fan-out were included for post-hybridization testing purposes. The wirebonding pads of these test detectors were soldered to a coaxial cable and tested using Stanford Research Systems SR-570, the output of which was monitored by an Agilent multimeter for dark and photo DC measurements, and a Stanford Research Systems SR-770 FFT Spectrum Analyzer for noise. The power spectral noise was measured at 2.5 kHz, which is below the bandwidth of the devices (3.6 kHz) and well above the 1/f noise knee.

The hybridized devices showed responsivity of more than 2500 A/W (2000 electrons/photon) at 1 V [see Fig. 3(a)], which is lower than the maximum responsivity values achieved by nanoinjection mechanism [11]. We attribute this change to the additional steps in processing flow required for hybridization.

The sample was placed in the custom-built visible/infrared microscope setup with an average optical power of 5 nW incident on the sample. The laser spot size was about 2 μm and was scanned over the sample using motorized drivers with nanometer-scale resolution through Labview. Based on this measurement, the devices had an active diameter of 30 μm leading to a fill factor of 78% (see Fig. 4).

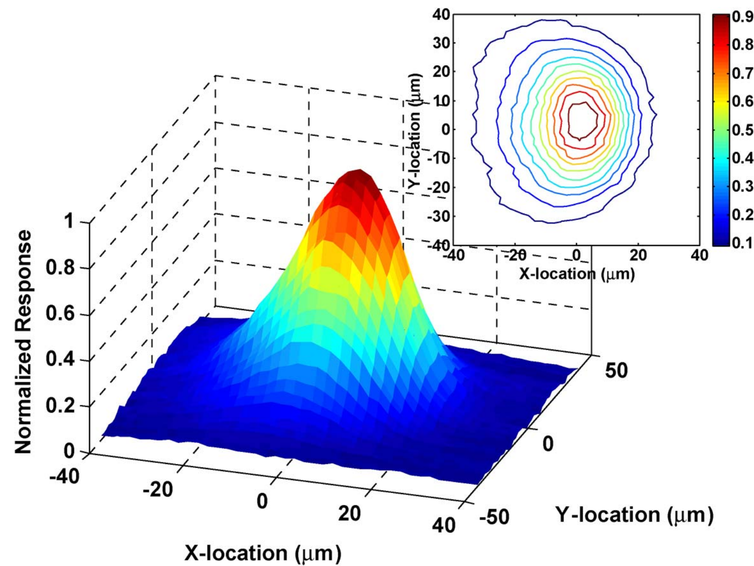

Fig. 4. Spatial photo-response plot of the device at room temperature and $\lambda = 1550$ nm. In inset shows the contour plot of the responsivity map.

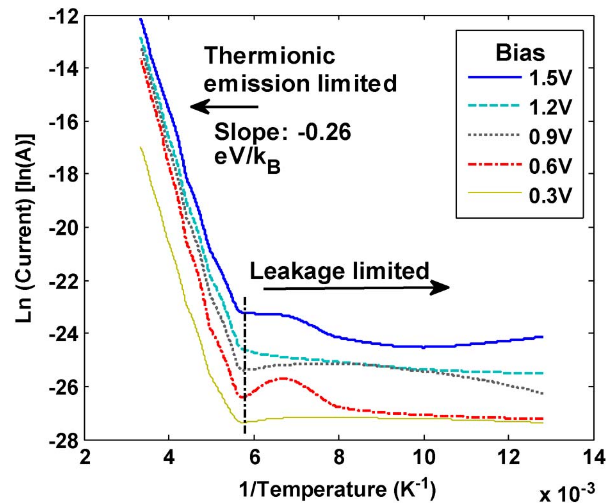

Fig. 5. Arrhenius plot of the internal dark current versus temperature at different bias voltages. The slope above 175 K indicates that the activation energy is 0.26 eV, which is in agreement with the InP-GaAsSb injection barrier height of ∼0.25 eV.

In our previous experiments [15] with the nanoinjection mechanism, we had observed low excess noise due to Fano noise suppression, which stems from temporal correlations between injected electrons due to the negative feedback inside the device. This leads to carrier antibunching that lowers the noise to sub-Poissonian levels. At internal amplification values between 1200 and 1600, we measured $F \sim 1.5$ [see Fig. 3(b)], which is unusually low for an imager with such high internal amplification.

The internal dark current (before amplification) of the hybridized test pixels was evaluated from 300 K down to 78 K (see Fig. 5). Above 175 K, the Arrhenius plot indicates that activation energy is 0.26 eV, which is in agreement with the InP-GaAsSb injection barrier height of ∼0.25 eV

Fig. 6. Short-wave infrared image taken using the nano-injection imager. The nano-injection imager is cooled to 200 K. The subject was standing in a completely dark room, holding a soldering iron at around 350 °C.

[16]. Below 175 K, a temperature-independent dark current was observed, which can be due to surface leakage or tunneling through the barrier.

For infrared imaging, the nanoinjection image chip was put in an evaluation kit from Indigo and was cooled to 200 K. The integration time was set to 0.5 ms, and f/1.8 lenses were used for both cameras. Images were acquired in a completely dark room. The scene was illuminated in infrared spectrum by a small soldering iron held by the subject while infrared images were taken (see Fig. 6).

4. Conclusion

In conclusion, we have designed and fabricated a nanoinjection-based SWIR imager, which has 320×256 pixel resolution with a pixel pitch of 30 μm. The imager pixels have responsivity of more than 2500 A/W, corresponding to a generation of more than 2000 electrons/photon at 1 V. The imager pixels exhibit very low excess noise factor at around 1.5 at high responsivity values between 1500 and 2000 A/W (i.e., 1200 to 1600 electrons/photon). The temperature behavior of the internal dark current (before amplification) was also studied, from which it was deduced that the injection process is limited by the barrier energy of 0.26 eV. SWIR pictures from the nanoinjection imager were acquired in a dark room where the subject held a hot soldering iron. In addition to the merits of the nanoinjection mechanism for individual detectors, these results show that the nanoinjection mechanism can easily be implemented in imagers to provide detector-level internal amplification while maintaining low noise levels and CMOS compatibility.

References

[1] I. A. Demarco, A. Periasamy, C. F. Booker, and R. N. Day, "Monitoring dynamic protein interactions with photoquenching FRET," *Nat. Methods*, vol. 3, no. 7, pp. 519–524, Jul. 2006.
[2] Y. Du, X. H. Hu, M. Cariveau, X. Ma, G. W. Kalmus, and J. Q. Lu, "Optical properties of porcine skin dermis between 900 nm and 1500 nm," *Phys. Med. Biol.*, vol. 46, no. 1, pp. 167–181, Jan. 2001.
[3] D. S. Moore, "Recent advances in trace explosives detection instrumentation," *Sens. Imaging*, vol. 8, no. 1, pp. 9–38, May 2007.
[4] E. Diamanti, C. Langrock, M. M. Fejer, Y. Yamamoto, and H. Takesue, "1.5 μm photon-counting optical time-domain reflectometry with a single-photon detector based on upconversion in a periodically poled lithium niobate waveguide," *Opt. Lett.*, vol. 31, no. 6, pp. 727–729, Mar. 2006.
[5] R. H. Hadfield, "Single-photon detectors for optical quantum information applications," *Nat. Photon.*, vol. 3, no. 12, pp. 696–705, Dec. 2009.
[6] E. Knill, R. Laflamme, and G. J. Milburn, "A scheme for efficient quantum computation with linear optics," *Nature*, vol. 409, no. 6816, pp. 46–52, Jan. 2001.

[7] T. P. Spiller, "Quantum information processing: Cryptography, computation, and teleportation," *Proc. IEEE*, vol. 84, no. 12, pp. 1719–1746, Dec. 1996.

[8] I. Hartl, X. D. Li, C. Chudoba, R. K. Ghanta, T. H. Ko, J. G. Fujimoto, J. K. Ranka, and R. S. Windeler, "Ultrahigh-resolution optical coherence tomography using continuum generation in an air-silica microstructure optical fiber," *Opt. Lett.*, vol. 26, no. 9, pp. 608–610, May 2001.

[9] R. Sloan, J. H. Shaw, and D. Williams, "Thermal radiation from the atmosphere," *J. Opt. Soc. Amer.*, vol. 46, no. 7, pp. 543–547, 1956.

[10] M. Vatsia, "Atmospheric Optical Environment," Research and Development, Army Night Vision Lab, Fort Belvoir, VA, Tech. Rep. ECOM-7023, 1972. [Online]. Available: http://oai.dtic.mil/oai/oai?verb=getRecord&metadataPrefix=html&identifier=AD0750610

[11] O. G. Memis, A. Katsnelson, S. C. Kong, H. Mohseni, M. Yan, S. Zhang, T. Hossain, N. Jin, and I. Adesida, "A photon detector with very high gain at low bias and at room temperature," *Appl. Phys. Lett.*, vol. 91, no. 17, p. 171 112, Oct. 2007.

[12] M. H. Devoret and R. J. Schoelkopf, "Amplifying quantum signals with the single-electron transistor," *Nature*, vol. 406, pp. 1039–1046, 2000.

[13] P. J. Edwards, "Sub-Poissonian electronic and photonic noise generation in semiconductor junctions," *Aust. J. Phys.*, vol. 53, no. 1, pp. 179–192, Jan. 2000.

[14] J. C. Campbell, S. Demiguel, M. Feng, A. Beck, G. Xiangyi, W. Shuling, Z. Xiaoguang, L. Xiaowei, J. D. Beck, M. A. Kinch, A. Huntington, L. A. Coldren, J. Decobert, and N. Tscherptner, "Recent advances in avalanche photodiodes," *IEEE J. Sel. Topics Quantum Electron.*, vol. 10, no. 4, pp. 777–787, Jul./Aug. 2004.

[15] O. G. Memis, A. Katsnelson, S. C. Kong, H. Mohseni, M. Yan, S. Zhang, T. Hossain, N. Jin, and I. Adesida, "On the source of jitter in a room-temperature nanoinjection photon detector at 1.55 μm," *Opt. Express*, vol. 16, no. 17, p. 12 701, 2008.

[16] C. R. Bolognesi, M. W. Dvorak, N. Matine, O. J. Pitts, and S. P. Watkins, "Ultrahigh performance staggered lineup ('Type-II') InP/GaAsSb/InP NpN double heterojunction bipolar transistors," *Jpn. J. Appl. Phys.*, vol. 41, no. 2B, p. 1131, Feb. 2002.